JOURNAL OF AIRCRAFT
Vol. 30, No. 3, May–June 1993

Comparison of Two Navier-Stokes Codes for Simulating High-Incidence Vortical Flow

Neal M. Chaderjian*
NASA Ames Research Center, Moffett Field, California 94035

Computations from two Navier-Stokes codes, NSS and F3D, are presented for a tangent-ogive cylinder body at high angle of attack. Features of this steady flow include a pair of primary vortices on the leeward side of the body, as well as secondary vortices. The topological and physical plausibility of this vortical structure is discussed. The accuracy of these codes are assessed by comparison of the numerical solutions with experimental data. The effects of turbulence model, numerical dissipation, and grid refinement are presented. The overall efficiency of these codes are also assessed by examining their convergence rates, computational time per time step, and maximum allowable time step for time-accurate computations. Overall, the numerical results from both codes compared equally well with experimental data, however, the NSS code was found to be significantly more efficient than the F3D code.

Introduction

THERE has been considerable interest by government agencies and industry to fly modern tactical fighters at high angles of attack. This very complex flow regime includes streamwise and crossflow separation, vortex asymmetry, and vortex burst phenomena which are inherently nonlinear and often time dependent. The vortical flow structures provide additional nonlinear lift which improves the aircraft maneuverability and agility. Although certain performance gains are realized in this flight regime, the vortices themselves can produce some adverse side affects. For example, departure from controlled flight can result from a combination of large forces generated by the onset of asymmetric forebody vortices and reduced yaw power.[1] Another example is the tail buffet phenomenon[2] experienced by twin-tail fighter aircraft which results from an interaction of wing/body vortices with the vertical tails. Vortex asymmetries interacting with an aircraft's motion can also lead to wing rock,[3] a sustained periodic motion in pitch and roll. These situations can restrict the aircraft's flight envelope, reduce its structural service life, and reduce pilot effectiveness.

The nonlinearities and unsteadiness mentioned above pose certain challenges to accurately predict and understand these phenomena. Wind-tunnel experiments tend to provide force and moment data and flow visualization information, but often lack detailed surface pressure data. These experiments are most often performed at subscale Reynolds numbers, and the time-dependent nature of the flow can offer special challenges to experimental accuracy and repeatability. Full-scale flight tests provide data at flight Reynolds numbers, but can also experience similar difficulties encountered by ground-based experiments. Computational fluid dynamics (CFD) utilizes powerful supercomputers to provide very detailed information about the flowfield. This can be very useful for analysis purposes, however, these computations can take large amounts of computer time and care must be taken to properly model the fluid turbulence. Other factors such as grid resolution and artificial dissipation can also affect the accuracy of the simulation. Each of these approaches should be fully utilized to advance the state-of-the-art in high-alpha aerodynamics. This combined approach is being utilized by the NASA high-alpha technology program.

At NASA Ames Research Center, the F3D Navier-Stokes code has been successfully used to predict steady and time-dependent flows about delta wings,[4] bodies of revolution,[5–7] aircraft forebodies[8] and aircraft geometries[9–11] at high incidence. The F3D code utilizes a combined upwind/central difference implicit algorithm and can treat complex geometries[9–11] with the Chimera[12] grid embedding approach. Comparisons with experimental data have, in general, been good. Although it has been demonstrated to give accurate predictions, one concern about this code is that it tends to be computationally more costly than several other Navier-Stokes methods. The Navier-Stokes simulation (NSS) code, formerly transonic Navier-Stokes (TNS), provides a more efficient alternative. This code uses an implicit, diagonalized, central-difference algorithm which is robust and has a lower operation count per time step. The NSS code has been used to simulate steady transonic viscous flow[13] about the complete F-16A fighter aircraft. These computations were performed for low to moderate angles of attack, and comparisons with experimental data were good. Treatment of complex geometries is accomplished by a zonal grid approach. Time-accuracy of the method has also been demonstrated in Ref. 14.

Subsonic, unsteady, high-alpha flow computations require large computational resources and computer time. Therefore, it is important to have an accurate and efficient numerical method. This article compares the accuracy and efficiency of the F3D and NSS codes for computing high incidence, high Reynolds number, turbulent flow about a tangent-ogive cylinder body of revolution. The following sections contain a description of the governing equations, turbulence model, numerical algorithms, and computational grids. Numerical results for the tangent-ogive cylinder at high angle of attack are presented in the results section, and their accuracy is assessed by comparison with experimental data[15] obtained by Lamont. The effects of turbulence model, grid resolution, and numerical dissipation on solution accuracy are addressed. The overall efficiencies of the two codes are also discussed.

Theoretical Background

Governing Equations

The time-dependent, Reynolds-averaged, Navier-Stokes (RANS) equations are used to simulate high-incidence vortical flow about a tangent-ogive cylinder. For the high Rey-

Presented as Paper 91-0175 at the AIAA 29th Aerospace Sciences Meeting, Reno, NV, Jan. 7–10, 1991; received April 13, 1991; revision received May 14, 1992; accepted for publication May 14, 1992.

*Research Scientist, Applied Computational Fluids Branch. Member AIAA.

nolds number flows considered in this article, the thin-layer approximation[16,17] is employed together with body-fitted curvilinear coordinates. Assuming a general coordinate transformation from physical space (x, y, z) to computational space (ξ, η, ζ), and that viscous terms are only important in the body-normal ζ-coordinate direction, the governing vector equations can be expressed in the following strong conservation law form:

$$\partial_\tau \hat{Q} + \partial_\xi \hat{E} + \partial_\eta \hat{F} + \partial_\zeta \hat{G} = Re^{-1}\partial_\zeta \hat{S} \qquad (1)$$

where $\hat{Q} = 1/J(\rho, \rho u, \rho v, \rho w, e)$ is the vector of dependent variables. This vector consists of ρ the fluid density, (u, v, w) the Cartesian velocity components, e the total energy per unit volume, and J the determinant of the coordinate-transformation Jacobian. The inviscid flux vectors $\hat{E}$, $\hat{F}$, and $\hat{G}$ correspond to the ξ, η, and ζ directions, respectively, and $\hat{S}$ is the thin-layer viscous flux vector. The perfect gas law, Sutherland's viscosity law, and a turbulence model completes the RANS system of equations. For viscous flow computations, no-slip and adiabatic wall boundary conditions are imposed at solid surfaces. Freestream conditions are imposed at far-field boundaries, while zero-gradient conditions are imposed at outflow boundaries. Further details describing the governing equations and boundary conditions can be found in Ref. 14.

Turbulence Model

The high incidence, high Reynolds number, turbulent flow considered in this article has significant crossflow separation on the leeward side of the tangent-ogive cylinder body, and therefore, requires a suitable turbulence model. A typical flow structure in the crossflow plane of a body at high angle of attack is shown in Fig. 1. The flow structure on the leeward side of the body can be viewed as a series of attached boundary layers below a vortex structure. The vortex structure itself consists of rolled-up shear layers whose vorticity was generated within the attached boundary layers. These vortices are essentially inviscid in nature so their vorticity is convected downwind and the effects of vorticity production or dissipation are very small and can be ignored. Although Fig. 1 draws attention to a crossflow plane, the flow is primarily directed downwind along the body axis. So if the windward flow is turbulent, the leeward boundary layers should also be turbulent, and the use of a turbulence model in this region is justified.

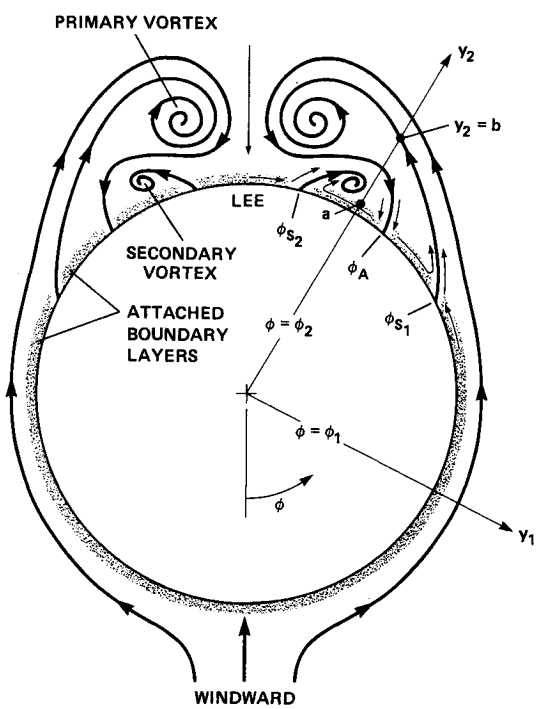

Fig. 1 Typical flow structure in the crossflow plane.[18]

The Baldwin-Lomax algebraic model[16] together with the Degani-Schiff modification[18,19] has proven to be an efficient isotropic eddy-viscosity model that properly accounts for the crossflow separation. The unmodified Baldwin-Lomax model performs well on the windward side where the flow is attached, but does not adequately model the crossflow separation on the leeward side. This model uses a two-layer approach for modeling a turbulent boundary layer. The failure on the leeward side is attributed to the length scale chosen by the outer-layer model. The length scale is chosen by determining where the function

$$F(y) = y|\omega(y)|[1 - \exp(-y^+/A^+)] \qquad (2)$$

is a maximum. In the above expression, y is the distance normal to the body, $|\omega(y)|$ is the magnitude of vorticity at y, y^+ is a nondimensional form of y, and A^+ is a constant. Typical behavior of $F(y)$ along a windward ray, e.g., $\phi = \phi_1$ in Fig. 1, is shown in Fig. 2a. The length scale y_{max} is easily found by determining where the function is a maximum. This value of y_{max} realistically represents the size of the turbulent boundary layer. The turbulent eddy viscosity is then determined from this length scale. Figure 2b shows the behavior of $F(y)$ along a ray on the leeward side of the body, e.g., $\phi = \phi_2$ in Fig. 1. The first peak corresponds to a length scale characteristic of the boundary layer, whereas the second peak corresponds to the vortex shear layer. The length scale associated with the second peak can be one or two orders of magnitude too large and effectively wash out all but the most dominant vortex structures. Degani and Schiff[18,19] recognized this and introduced logic to identify the first peak, and hence, give a length scale that is realistic for the boundary layer. One complication does occur, however, when searching along a ray that is near a separation point, e.g., $\phi = \phi_{s_1}$ in Fig. 1. In this case both peaks merge together making it difficult to locate the first peak and result in a length scale that is once again too large. This problem was circumvented by specifying a cutoff distance (y_{cutoff}) that limits the radial search distance

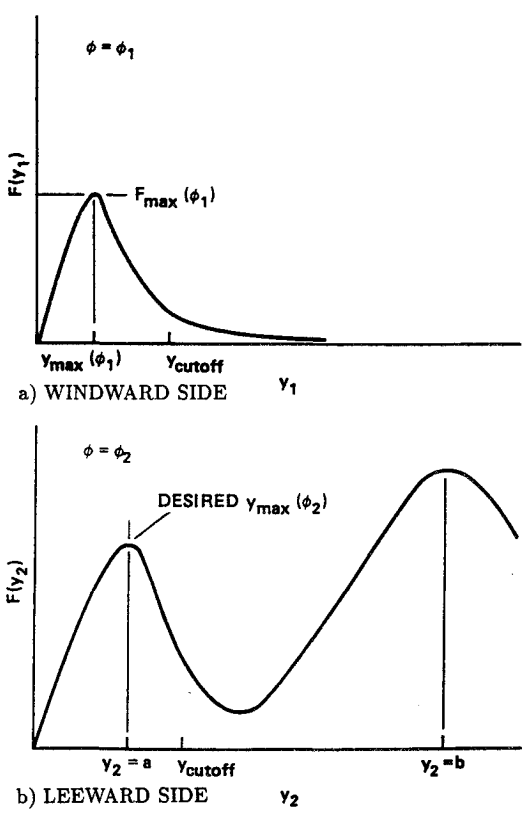

Fig. 2 Behavior of $F(y)$ at large angles of attack.[18]

for y_{max} to a value appropriate for a boundary layer. If, while searching along an outward ray, no local maximum is found within the cutoff distance, then y_{max} is locally frozen to the value obtained at the previous circumferential location in the windward direction. The cutoff distance is determined from the relation

$$y_{cutoff} = Cy_{max}|_w \tag{3}$$

where $y_{max}|_w$ is the value of y_{max} at the windward plane of symmetry, and C is a user-specified cutoff constant. The cutoff constant is usually of the order $C \sim 3$–5. Further details of the Baldwin-Lomax model with the Degani-Schiff modification can be found in Refs. 18 and 19.

All viscous computations presented in this article assume fully turbulent flow beginning at the nose of the tangent-ogive cylinder body, i.e., transitional effects are ignored. This approximation is consistent with the high Reynolds number assumption.

Numerical Algorithms

NSS Code

The NSS code uses an implicit, approximately factored, central-difference algorithm to integrate Eq. (1). This algorithm is a diagonal form of the Beam-Warming algorithm[20] due to Pulliam and Chaussee.[21] The spatial derivatives use second-order accurate central differencing throughout, with artificial dissipation added to damp high frequency errors. The artificial dissipation terms used in the diagonal algorithm consist of blended second-order and fourth-order differences. The use of implicit fourth-order artificial dissipation dictates the solution of a scalar pentadiagonal system of equations. Solution of this scalar system of equations requires a significantly smaller number of computational operations per time step than methods solving a block tridiagonal system, e.g., the Beam-Warming algorithm. This method is limited to first-order time accuracy (unless a Newton subiteration procedure is used).

The implicit and explicit dissipation terms used in the NSS code are identical and have been modified to reduce the dissipation within the boundary layer. The dissipation operator in the ζ-coordinate direction is given by

$$D|_\zeta = \nabla_\zeta [(\psi_n f_n/J)_{l+1} + (\psi_n f_n/J)_l] \\ [\varepsilon^{(2)}\Delta_\zeta - \varepsilon^{(4)}\Delta_\zeta\nabla_\zeta\Delta_\zeta]J \tag{4}$$

where

$$\psi_n = |U| + c\sqrt{\xi_x^2 + \xi_y^2 + \xi_z^2} \\ + |V| + c\sqrt{\eta_x^2 + \eta_y^2 + \eta_z^2} \\ + |W| + c\sqrt{\zeta_x^2 + \zeta_y^2 + \zeta_z^2} \tag{5}$$

$$f_n = \min\{1.0,\ 0.1 + 0.9[(u^2 + v^2 + w^2)/M_\infty^2]\} \tag{6}$$

$$\varepsilon^{(2)} = K_2\,[\tfrac{1}{2}\Upsilon_l + \tfrac{1}{4}(\Upsilon_{l+1} + \Upsilon_{l-1})] \tag{7a}$$

$$\varepsilon^{(4)} = K_4 - \min(K_4,\ \varepsilon^{(2)}) \tag{7b}$$

$$\Upsilon_l = \left|\frac{P_{l+1} - 2P_l + P_{l-1}}{P_{l+1} + 2P_l + P_{l-1}}\right| \tag{7c}$$

In Eqs. (4–7), Δ_ζ and ∇_ζ correspond to two-point forward and backward difference operators respectively, P is the static pressure, and M_∞ is the freestream Mach number. The parameter ψ_n is the sum of the spectral radii of the Jacobian matrices $\partial\hat{E}/\partial\hat{Q}$, $\partial\hat{F}/\partial\hat{Q}$, and $\partial\hat{G}/\partial\hat{Q}$. Furthermore, U, V, and W are the contravariant velocity components in the ξ, η, and ζ directions, c is the local speed of sound, and terms such as ξ_x, ξ_y, ξ_z, . . . are coordinate transformation metrics. The parameter f_n, [Eq. (6)] reduces the artificial dissipation within the boundary layer so as not to dominate over the physical dissipation. The switching operators $\varepsilon^{(2)}$ and $\varepsilon^{(4)}$ determine the type of smoothing, i.e., second-order dissipation near large pressure gradients and fourth-order dissipation elsewhere. The fourth-order dissipation reduces to a second-order term near grid boundaries. Typical values for the dissipation constants are $K_2 = 0.25$ and $K_4 = 0.005$. Dissipation in the ξ and η directions are similar to Eqs. (4–7). Further details of this algorithm can be found in Ref. 14.

F3D Code

An implicit approximately factored algorithm is used in the F3D Code. This two-factor scheme, developed by Steger et al.,[22] employs flux-vector splitting in the ξ direction (nominally the streamwise direction) and central differencing in the η and ζ directions (nominally the crossflow and body-normal directions). The thin-layer viscous terms are treated implicitly. This scheme is second-order accurate in space and first- or second-order accurate in time. The second-order option was used in this article.

Artificial dissipation is added in the crossflow (η and ζ) directions to damp high-frequency errors. A blended second- and fourth-order dissipation is used on the explicit side, and second-order dissipation is used on the implicit side. Consequently, this algorithm requires the solution of a block tridiagonal system of equations.

The blended explicit dissipation in the ζ direction is given by

$$D_e|_\zeta = \nabla_\zeta \left\{\frac{\varepsilon}{2}\left[\left(\frac{\psi_f}{J}\right)_{l+1} + \left(\frac{\psi_f}{J}\right)_l\right] \times \left[\frac{1}{2}(\alpha_{l+1} + \alpha_l)\Delta_\zeta \right.\right. \\ \left.\left. - \left(\frac{1}{1 + \alpha_{l+1} + \alpha_l}\right)\Delta_\zeta\nabla_\zeta\Delta_\zeta\right]J\right\} \tag{8}$$

where

$$\psi_f = |W| + \sqrt{(\zeta_x^2 + \zeta_y^2 + \zeta_z^2)\tilde{c}^2 + 0.01} \tag{9}$$

$$\alpha = (1 + M_\infty^\gamma)\left|\frac{P_{l+1} - 2P_l + P_{l-1}}{P_{l+1} + 2P_l + P_{l-1}}\right| \tag{10}$$

The dissipation coefficient typically has a value $\varepsilon = 0.03$. The modified spectral radius (ψ_f) is reduced in the boundary layer by the parameter $\tilde{c}^2 = (u^2 + v^2 + w^2)/M_\infty^2$. The explicit dissipation in the η-direction is similar to the above formulas with the exception that $\tilde{c}^2 = c^2$, the square of the local speed of sound. Further details of this algorithm can be found in Ref. 22.

Although the explicit dissipations for the NSS and F3D codes differ in details, they have essentially the same form. The primary differences between the dissipations is in the way they reduce the spectral radius in the boundary layer, and the NSS spectral radius is isotropic while the F3D spectral radius is dependent on the coordinate direction.

Local Time Step

A locally-varying time step is used to accelerate the rate of convergence of both the NSS and F3D codes for steady flow computations. The time step varies with the local grid cell volume, and is given by

$$\Delta t = \Delta t_0[(1 + \varepsilon_r\sqrt{J})/(1 + \sqrt{J})] \tag{11}$$

where Δt_0 and ε_r are positive constants, and J is the Jacobian of the coordinate transformation. This expression reduces the time step when grid cell volumes are small (large coordinate Jacobians) and increases it for large volumes (small coordinate

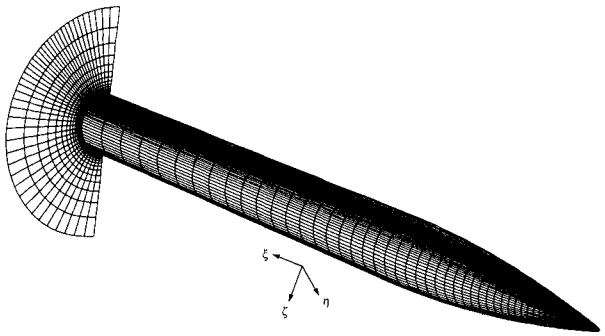

Fig. 3 Spherical grid for a tangent-ogive cyclinder body (59 × 91 × 50). Every other circumferential point is removed for viewing clarity.

Jacobians). The parameter ε_r limits the time step when the grid volumes become too small, e.g., near the axis of a spherical grid, otherwise it can be set to zero.

Computational Grids

Three spherical grids have been generated for the tangent-ogive cylinder body corresponding to the experimental model of Lamont.[15] A hyperbolic grid-generation method was used, with exponential clustering near the body surface to resolve the boundary-layer gradients. The coarsest grid used in this study has 59 points in the streamwise ξ direction, 61 points in the circumferential η direction, and 50 points in the body-normal ζ direction, for a total of ~180,000 points. An additional plane of points is added near the windward and leeward planes of symmetry to impose symmetric flow boundary conditions. The grid has uniform spacing in the circumferential direction, corresponding to $\Delta\phi = 3$ deg. A medium-density grid was obtained by doubling the circumferential resolution of the coarse grid to 59 × 123 × 50 points (~360,000 total). This corresponds to a uniform circumferential spacing of $\Delta\phi = 1.5$ deg. A third grid was generated having 59 × 91 × 50 points (~270,000 total) as shown in Fig. 3. (Every other grid point in the circumferential direction has been removed from Fig. 3 for clarity.) This grid is identical to the coarse grid on the windward side of the body, but has circumferentially clustered grid points on the leeward side. A circumferential spacing of $\Delta\phi = 1$ deg was obtained at $\phi = 135$ deg measured from the windward symmetry plane. Therefore, this grid has greater circumferential resolution in the region of crossflow separation than the medium grid. This circumferentially clustered grid will be referred to as the fine grid throughout this article. All three grids have identical spacing in the axial and body-normal directions.

Results

Wind-Tunnel Experiment

The numerical computations presented in this article were carried out at flow conditions corresponding to an experiment reported by Lamont.[15] This experiment was conducted in the NASA Ames 12-ft pressure wind tunnel, where it is possible to achieve high Reynolds number flow. A rigid tangent-ogive cylinder body was mounted on a crossbar/counterweight assembly which is capable of rotating the body to large angles of attack. The forebody merges into the cylindrical section 3.5-diam downwind of the nose. (Figure 3 shows a computational grid for the tangent-ogive cylinder body.) Circumferential pressure data was obtained from a ring of orifices located every $X/D = 0.5$ over the range $0.5 \leq X/D \leq 6.0$, where X is the axial distance from the nose of the body, and D is the diameter of the cylinder section. Each ring of orifices provided a check for flow asymmetry. Although the surface pressure data was quite extensive, no surface flow visualization was attempted. For further details, refer to Ref. 15.

Comparison of Computation and Experiment

All computations reported in this article correspond to the tangent-ogive cylinder body at freestream Mach number $M_\infty = 0.20$, angle of attack $\alpha = 20.0$ deg, and Reynolds number based on the cylinder diameter $Re_D = 5.0 \times 10^6$. Under these conditions the experimental data indicates steady symmetric flow. Consequently, only half-body grids were used and symmetry plane boundary conditions imposed, e.g., see Fig. 3. The turbulence model cutoff constant [Eq. (3)] was set to $C = 5.0$ and the fine grid (59 × 91 × 50) was used in all computations unless otherwise noted.

Density and helicity density contours computed by the NSS code are shown in Fig. 4 at a crossflow plane located at $X/D = 6.0$. (Computations by the F3D code indicate contour patterns that are very similar to the NSS contours shown in Fig. 4.) The solid lines of helicity density in Fig. 4b correspond to a clockwise rotation and the shaded area to a counterclockwise rotation. It is evident from this that there are four vortical structures: two outer ones with a clockwise sense of rotation and two inner ones with a counterclockwise sense of rotation. The two outer vortices form a primary vortex pair, and the two inner vortices are secondary structures induced by the primary vortices. This vortex structure is also evident in the density contours shown in Fig. 4a. Similar primary vortex pairs have been noted experimentally on a tangent-ogive cylinder body with elliptic cross section by Ward and Katz,[23] on a missile body by Pagan and Molton,[24] and computationally on a hemisphere-cylinder body by Ying et al.[25]

Figure 5 shows computed surface flow patterns on the tangent-ogive cylinder body which were obtained by using the NSS and F3D codes. These patterns were constructed by computing particle paths that are constrained to a surface of grid points one point above the body in the body-normal direction. The separation line located closest to the windward side is called the line of primary crossflow separation, and corresponds to the primary vortex pair. The second and third separation lines correspond to the two secondary vortices. Over-

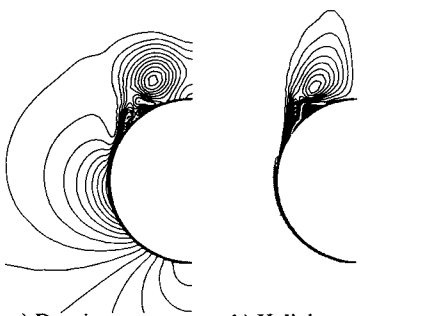

a) Density contours b) Helicity contours

Fig. 4 Computed NSS crossflow structure on the tangent-ogive cylinder body at $X/D = 6.0$. $M_\infty = 0.20$, $\alpha = 20.0$ deg, and $Re_D = 5.0 \times 10^6$.

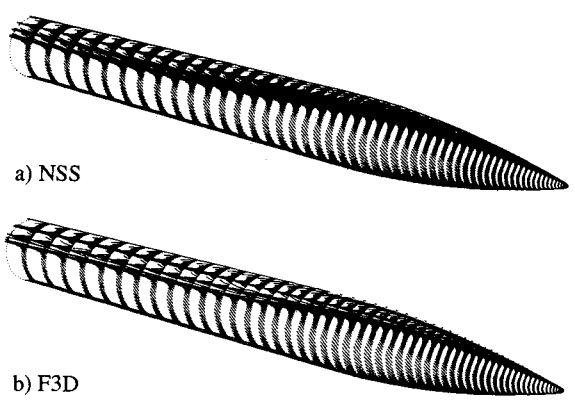

a) NSS

b) F3D

Fig. 5 Computational surface flow patterns for the tangent-ogive cylinder body. $M_\infty = 0.20$, $\alpha = 20.0$ deg, and $Re_D = 5.0 \times 10^6$.

all, the surface flow patterns predicted by the NSS and F3D codes are very similar to each other. Each code predicted three separation lines, and the lines of separation on the forward portion of the body have the same location and curvature. The separation patterns predicted by both codes on the aft portion of the body are also similar to each other, but there are some minor differences. The primary separation line predicted by F3D is slightly closer to the windward side than the primary separation line predicted by the NSS code. The reattachment lines in the F3D computation are located approximately midway between the separation lines while the NSS reattachment lines are more obscure, being located very close to the separation lines.

Figure 6 is a sketch interpreting the crossflow topology at $X/D = 6.0$. The reattachment and separation locations alternate on the body surface. The primary vortex pair is interpreted as forming from the shear layer that leaves the body at the first separation line. There is also a saddle point singularity between the two primary vortices. This flow structure is topologically correct and consistent with Figs. 4 and 5. From a physical point of view, the flow topology in Fig. 6 can form in the following manner. The outermost primary vortex (i.e., the one closest to the leeward symmetry plane) first forms near the tangent-ogive cylinder nose. The shear layer feeding into this vortex originates from the separation line closest to the windward side. As this vortex increases in strength along the length of the body, the secondary vortex forms. This corresponds to the separation line closest to the leeward symmetry plane. Proceeding downwind along the length of the body, the primary vortex shear layer can warp and eventually roll up into the second primary vortex (i.e., the one closer to the body surface). So the primary separation shear layer is seen to roll up into two primary vortices. Proceeding farther downwind along the body, the second primary vortex becomes strong enough to form the second secondary vortex. This corresponds to the second (middle) line of separation on the body. Therefore, the crossflow topology in Fig. 6 is topologically correct and physically plausible.

Figure 7 compares the pressure coefficients (C_p) computed with the NSS and F3D codes with experimental values at three axial locations. The circumferential angle $\phi = 0$ deg corresponds to the windward symmetry plane, while $\phi = 180$ deg corresponds to the leeward symmetry plane. The tangent-ogive cylinder body does not have any sharp edges, so the surface pressures on the leeward side are sensitive to the crossflow separation topology, and therefore, provide a good measure of computational accuracy. Overall, the C_p computed by both codes compare well with each other and with the experimental data, although the F3D code seems to predict larger suction peaks associated with the crossflow vortices on the leeward side than those predicted by the NSS code. Both codes underpredict the pressure coefficient on the windward side. This is surprising since both codes do so well on the leeward side (where there is significant crossflow separation), and not as well on the windward side (where the flow is attached and less sensitive to the turbulence model). In view of this fact, it is possible that the experimental pressures could be reading a bit high, perhaps due to flow entering the windward ports at high angle-of-attack conditions. This would result in pressure measurements somewhere between the static and total values. It is unclear whether the discrepancy is due to the experiment or the computations. Nevertheless, both NSS and F3D appear to do an equally good job of predicting the experimental pressures and compare well with each other.

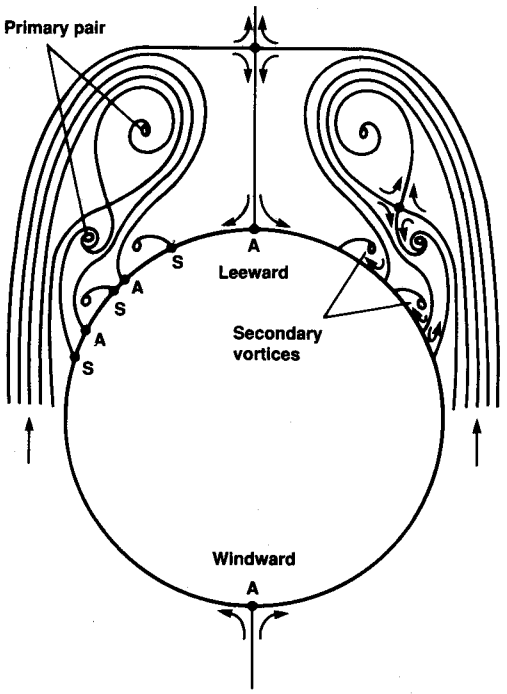

Fig. 6 Sketch of flow structure in a crossflow plane at $X/D = 6.0$. $M_\infty = 0.20$, $\alpha = 20.0$ deg, and $Re_D = 5.0 \times 10^6$.

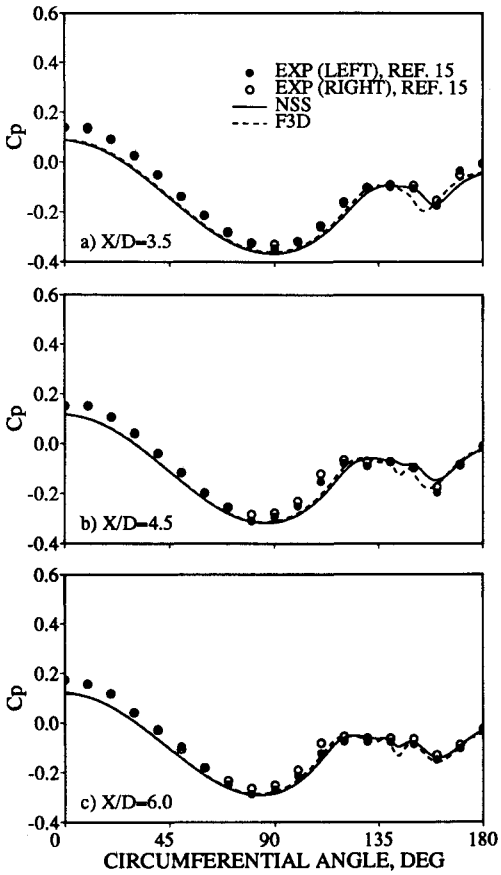

Fig. 7 Comparison of pressure coefficients computed by NSS and F3D with experiment. $M_\infty = 0.20$, $\alpha = 20.0$ deg, $Re_D = 5.0 \times 10^6$ (computation), and $Re_D = 4.0 \times 10^6$ (experiment).

Turbulence Model Effects

The Baldwin-Lomax model with the Degani Schiff modification is used throughout this article. The cutoff constant [Eq. (3)] was initially set to $C = 3.0$. The effect of grid refinement on the F3D pressure coefficients is shown in Fig. 8. Recall that the $59 \times 91 \times 50$ grid has the finest circumferential resolution on the leeward side due to grid clustering. As the grid is refined, the suction peaks on the leeward side increase in magnitude and move outboard away from the leeward symmetry plane. One would expect the solution to improve with grid refinement and converge to some result. By increasing the cutoff constant to $C = 5.0$, the suction peaks are reduced. A pressure coefficient comparison com-

puted on the fine grid with these two cutoff values is shown in Fig. 9. Notice that the computed pressure coefficients (with $C = 5.0$) compare very well with the experimental data. The reason the suction peaks increased with increased grid resolution is because the cutoff constant was initially so small that the search for a turbulent length scale was terminated within the leeward side boundary layer. This caused an artificially small length scale, and consequently, the leeward side values of eddy viscosity were too low. By increasing the cutoff constant to $C = 5.0$, the entire boundary layer could be searched for an appropriate length scale. The Baldwin-Lomax model with the Degani-Schiff modification ordinarily does a good job modeling crossflow separation on bodies at high angle of attack, however, care must be taken in choosing the cutoff constant C. In practice the function $F(y)$ [Eq. (2)] should be examined to ensure C is large enough to accommodate the boundary-layer thickness on the leeward side. Figure 10 shows how the surface flow patterns computed by F3D are affected by the cutoff constant. There are four separation lines when $C = 3.0$, and three separation lines when $C = 5.0$. When $C = 3.0$, the increased suction peaks cause a tertiary vortex to form near the leeward symmetry plane. When $C = 5.0$, the tertiary vortex disappears and the first and second separation lines are displaced somewhat.

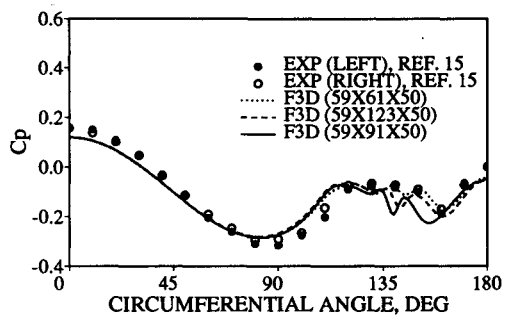

Fig. 8 Grid refinement effects on F3D pressure coefficients at $X/D = 5.0$. $M_\infty = 0.20$, $\alpha = 20.0$ deg, $Re_D = 5.0 \times 10^6$ (computation), and $Re_D = 4.0 \times 10^6$ (experiment), and $C = 3.0$.

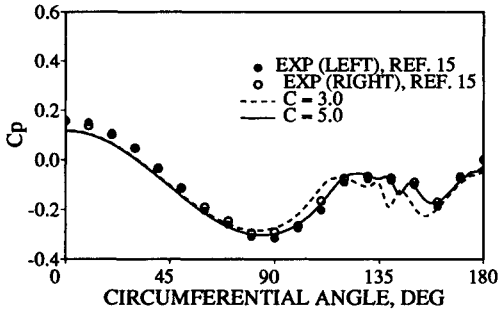

Fig. 9 Effect of different turbulent cutoff constants on F3D pressure coefficients at $X/D = 5.0$. $M_\infty = 0.20$, $\alpha = 20.0$ deg, $Re_D = 5.0 \times 10^6$ (computation), and $Re_D = 4.0 \times 10^6$ (experiment).

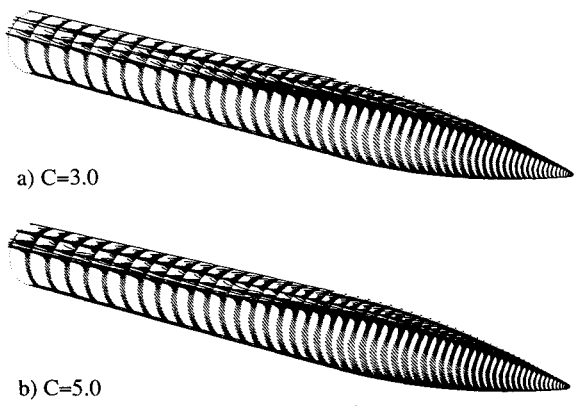

Fig. 10 Effect of different turbulent cutoff constants on F3D surface flow patterns. $M_\infty = 0.20$, $\alpha = 20.0$ deg, and $Re_D = 5.0 \times 10^6$.

The NSS code, with $C = 3.0$, did not experience the same growth of suction peaks with grid refinement as the F3D code. As the grid was refined, the solution converged to a result close to the experimental values. However, this does not mean that the pressure coefficients predicted by the NSS code were unaffected by the turbulent cutoff constant. Figure 11 shows how different cutoff constants affected the pressure coefficients computed by NSS. When the cutoff constant is set to $C = 5.0$, the computed C_p compare more favorably with experimental values than when $C = 3.0$. Although Figs. 9 and 11 show the same trends, the effect of different cutoff constants on computed C_p appear to be less pronounced with the NSS code than with F3D.

Artificial Dissipation Effects

F3D density contours at two axial locations are shown in Fig. 12. The fourth-order dissipation constant was set to $\varepsilon = 0.01$, see Eq. (8). This value was chosen because it was the smallest value of ε that maintained code stability for this case. The oscillations in the ζ-coordinate direction are apparent and are most pronounced near the nose of the tangent-ogive cylinder body. The F3D skin friction coefficient C_f on the windward symmetry plane, and at $X/D = 6.0$, differs from the NSS value by 4.6%. [The fourth-order dissipation constant for the NSS code, Eq. (7b), was $K_4 = 0.005$.] Increasing the dissipation coefficient to $\varepsilon = 0.03$ (see Fig. 13) removed the density oscillations. This also reduced the difference of C_f

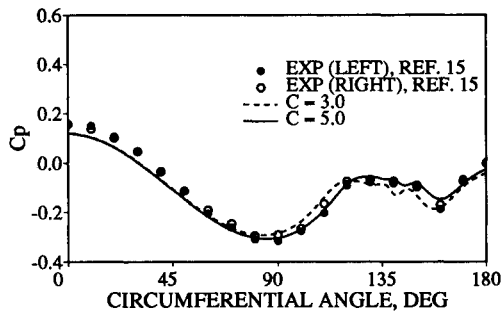

Fig. 11 Effect of different turbulent cutoff constants on NSS pressure coefficients at $X/D = 5.0$. $M_\infty = 0.20$, $\alpha = 20.0$ deg, $Re_D = 5.0 \times 10^6$ (computation), and $Re_D = 4.0 \times 10^6$ (experiment).

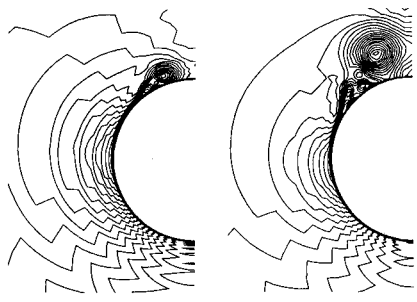

Fig. 12 F3D density contours with $\varepsilon = 0.01$. $M_\infty = 0.20$, $\alpha = 20.0$ deg, and $Re_D = 5.0 \times 10^6$.

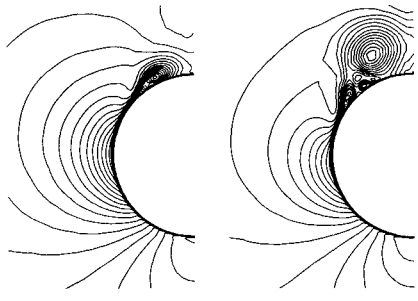

Fig. 13 F3D density contours with $\varepsilon = 0.03$. $M_\infty = 0.20$, $\alpha = 20.0$ deg, and $Re_D = 5.0 \times 10^6$.

between the two codes to 2.5%. The same trend of oscillatory density contours occurs with the NSS code when the fourth-order smoothing constant is lowered to $K_4 = 0.002$. Apparently the practice of using the smallest dissipation coefficient possible (while still maintaining code stability) does not necessarily give the most accurate results. When oscillations occur in the flow variables, the accuracy of computed quantities such as C_f are suspect. One should use the smallest dissipation coefficient possible that results in a solution that is free of oscillations.

Figure 14 compares the relative sizes of the NSS and F3D fourth-order dissipation coefficients. (The dissipation constants were set to $\varepsilon = 0.03$ and $K_4 = 0.005$ for F3D and NSS, respectively.) The ratio of the F3D and NSS dissipation coefficients are shown as a function of the body-normal index, L. Although this figure pertains to $X/D = 6.0$ and $\phi = 135$ deg, it is typical of the leeward side. Note that the dissipation for the NSS code is smaller than the F3D code for $L \leq 32$. As a point of reference, $L = 32$ corresponds to the top of the outermost vortex indicated in Fig. 4. In the outermost flow, $L \geq 33$, F3D has a lower dissipation than NSS. The primary difference between the two fourth-order dissipation terms is the manner in which the spectral radius is reduced within the boundary layer, see Eqs. (6) and (9).

Time Step Effects

The locally varying time step given by Eq. (11) is used to accelerate the rate of convergence to a steady state. A comparison of the convergence histories of the L_2-norm of the residual for the NSS and F3D codes are given in Fig. 15. Except for the initial 1000 iterations, the rate of convergence appears to be similar. It is interesting, however, to examine the convergence rates of C_p for the NSS code more closely. When $\varepsilon_\tau = 0$ ($\Delta t_0 = 5.0$), the L_2-norm initially drops more rapidly than when $\varepsilon_\tau = 0.0005$ ($\Delta t_0 = 2.0$). In the former case, C_p is converged on the aft portion of the tangent-ogive cylinder body in about 3000 iterations, whereas C_p near the nose requires about 7000 iterations, see Fig. 16. This occurs because Eq. (11) with $\varepsilon_\tau = 0$, gives too small a time step near the nose where the spherical grid has very small volumes. In the latter case C_p is more uniformly converged over the entire body in about 5500 iterations, see Fig. 16. The convergence of C_p for the F3D code is also relatively uniform along the tangent-ogive cylinder body with $\varepsilon = 0.005$ ($\Delta t_0 = 1.0$), and requires about 5500 iterations. So for steady flow with local time steps, both codes have about the same convergence rate. However, the F3D code requires about 2.3 times more computer time per time step than the NSS code, and is therefore less efficient. The NSS code required 16.5 μs/grid point/iteration on a Cray YMP, while the F3D code required 36.7 μs/grid point/iteration.

The maximum allowable constant time step for the NSS code to maintain stability, for this case, was $\Delta t = 0.01$. The corresponding value for F3D was $\Delta t = 0.005$, or half as much. Taking into account the smaller allowable time step and larger execution time per time step, the F3D code should require

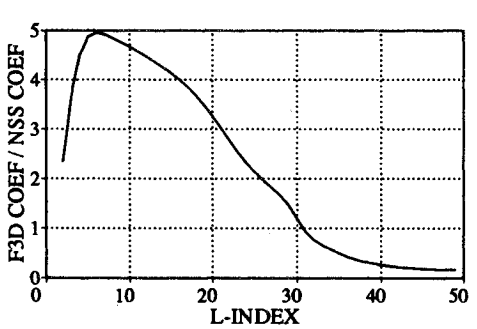

Fig. 14 Comparison of F3D and NSS fourth-order smoothing coefficients in the ζ direction at $X/D = 6.0$ and $\phi = 135$ deg. $M_\infty = 0.20$, $\alpha = 20.0$ deg, and $Re_D = 5.0 \times 10^6$.

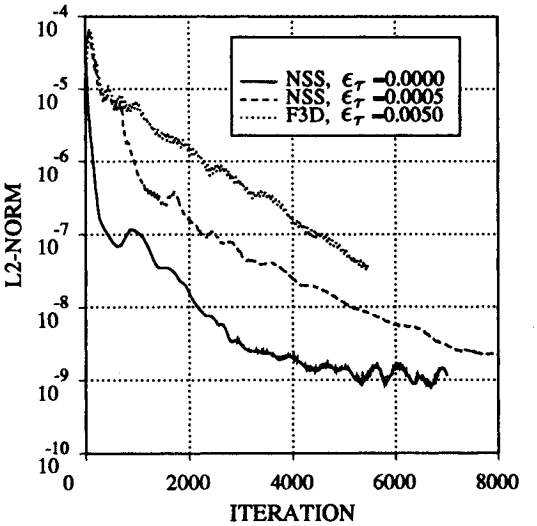

Fig. 15 Steady convergence history of the L_2-norm of the residual. $M_\infty = 0.20$, $\alpha = 20.0$ deg, and $Re_D = 5.0 \times 10^6$.

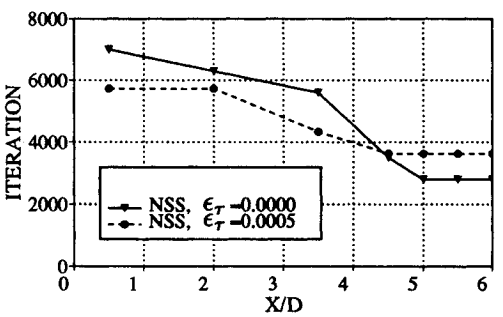

Fig. 16 Steady convergence history of the surface pressure coefficients. $M_\infty = 0.20$, $\alpha = 20.0$ deg, and $Re_D = 5.0 \times 10^6$.

4–5 times more computer time for a time-accurate computation than the NSS code. The maximum allowable time step permissible for each code will, of course, depend on the specific application, computational grid and the flow conditions.

Conclusions

Turbulent computations for a tangent-ogive cylinder body at high angle of attack have been presented using the thin-layer, Reynolds-averaged, Naview-Stokes codes NSS and F3D. The computed flow structures contained a primary vortex pair with secondary vortices. The pressure coefficients computed by both codes compared equally well with the experimental data. The Baldwin-Lomax eddy viscosity turbulence model with the Degani-Schiff modification accurately predicted the crossflow separation on the leeward side of the tangent-ogive cylinder body. The choice of the turbulent cutoff constant did affect the leeward pressure coefficients somewhat in both codes. The F3D code appeared to be more sensitive to changes in the turbulence cutoff constant than NSS. When the turbulent cutoff constant was too low, F3D tended to give increasingly large suction peaks on the leeward side as the grid was refined. The NSS code did not exhibit this behavior. Nevertheless, both codes gave equally accurate results when the proper turbulent cutoff constants were used. It was also demonstrated that the practice of using the lowest dissipation possible, while still maintaining code stability, can lead to spurious flow oscillations. When this happens, sensitive numerical quantities such as the skin-friction coefficient are suspect. One should use the smallest dissipation coefficient possible such that the numerical solution is free from oscillations.

The NSS code was shown to be more efficient than the F3D code. Results presented in this article indicate that the NSS and F3D codes have about the same convergence rates, but the F3D code requires 2.3 times more computer time per time

step than NSS. Moreover, for the case studied here, the NSS code allowed a constant time step that was twice as large as the one allowed by the F3D code. This suggests the F3D code could require 4–5 times more computer time for simulating time-accurate vortical flow.

References

[1]Tavella, D. A., Schiff, L. B., and Cummings, R. M., "Pneumatic Vortical Flow Control at High Angles of Attack," AIAA Paper 90-0098, Jan. 1990.

[2]Zimmerman, N. H., Ferman, M. A., Yurkovich, R. N., and Gerstenkorn, G., "Prediction of Tail Buffet Loads for Design Application," AIAA Paper 89-1378-CP, April 1989.

[3]Baucom, C. M., and Clark, C., "Navy Departure/Spin and Air Combat Maneuvering Evaluation of a National Aeronautics and Space Administration Developed Flight Control System for the F-14," *Twenty-Ninth Symposium Proceedings, The Society of Experimental Test Pilots*, ISSN 0742-3705, Beverly Hills, CA, Sept. 1985.

[4]Ekaterinaris, J. A., and Schiff, L. B., "Vortical Flows over Delta Wings and Numerical Prediction of Vortex Breakdown," AIAA Paper 90-0102, Jan. 1990.

[5]Degani, D., and Schiff, L. B., "Numerical Simulation of the Effect of Spatial Disturbances on Vortex Asymmetry," *AIAA Journal*, Vol. 29, No. 3, 1991, pp. 344–352.

[6]Degani, D., Schiff, L. B., and Levy, Y., "Numerical Prediction of Subsonic Turbulent Flows over Slender Bodies at High Incidence," *AIAA Journal*, Vol. 29, No. 12, 1991, pp. 2054–2061.

[7]Schiff, L. B., Degani, D., and Cummings, R. M., "Numerical Simulation of Separated Vortical Flows on Bodies at Large Angles of Attack," *Numerical and Physical Aspects of Aerodynamic Flows IV*, edited by T. Cebeci, Springer-Verlag, New York, 1990, pp. 205–222.

[8]Schiff, L. B., Cummings, R. M., Sorenson, R. L., and Rizk, Y. M., "Numerical Simulation of High-Incidence Flow over the Isolated F-18 Fuselage Forebody," *Journal of Aircraft*, Vol. 28, No. 10, 1991, pp. 609–617.

[9]Cummings, R. M., Rizk, Y. M., Schiff, L. B., and Chaderjian, N. M., "Navier-Stokes Predictions of the Flowfield Around the F-18 (HARV) Wing and Fuselage at Large Incidence," AIAA Paper 90-0099, Jan. 1990.

[10]Rizk, Y., Schiff, L., and Gee, K., "Numerical Simulation of the Viscous Flow Around the F-18 at High Angles of Attack," AIAA Paper 90-2999, Aug. 1990.

[11]Rizk, Y., Gee, K., and Schiff, L., "Numerical Prediction of the Flowfield Around the Complete F18 Aircraft at Large Incidence," AIAA Paper 91-0020, Jan. 1991.

[12]Benek, J. A., Buning, P. G., and Steger, J. L., "A 3-D Chimera Grid Embedding Technique," AIAA Paper 85-1523, July 1985.

[13]Flores, J., and Chaderjian, N. M., "Zonal Navier-Stokes Methodology for Flow Simulation About a Complete Aircraft," *Journal of Aircraft*, Vol. 27, No. 7, 1990, pp. 583–590.

[14]Chaderjian, N. M., and Guruswamy, G. P., "Unsteady Transonic Navier-Stokes Computations for an Oscillating Wing Using Single and Multiple Zones," AIAA Paper 90-0313, Jan. 1990.

[15]Lamont, P. J., "Pressures Around an Inclined Ogive Cylinder with Laminar, Transitional, or Turbulent Separation," *AIAA Journal*, Vol. 20, No. 11, 1982, pp. 1492–1499.

[16]Baldwin, B. S., and Lomax, H., "Thin Layer Approximation and Algebraic Model for Separated Turbulent Flow," AIAA Paper 78-257, Jan. 1978.

[17]Steger, J. L., "Implicit Finite-Difference Simulation of Flow About Arbitrary Two-Dimensional Geometries," *AIAA Journal*, Vol. 16, No. 7, 1978, pp. 679–686.

[18]Degani, D., and Schiff, L. B., "Computation of Supersonic Viscous Flows Around Pointed Bodies at Large Incidence," AIAA Paper 83-0034, Jan. 1983.

[19]Degani, D., and Schiff, L. B., "Computation of Turbulent Supersonic Flows Around Pointed Bodies Having Crossflow Separation," *Journal of Computational Physics*, Vol. 66, No. 1, 1986, pp. 173–196.

[20]Beam, R. M., and Warming, R. F., "An Implicit Finite-Difference Algorithm for Hyperbolic Systems in Conservation Law Form," *Journal of Computational Physics*, Vol. 22, 1976, pp. 87–110.

[21]Pulliam, T. H., and Chaussee, D. S., "A Diagonal Form of an Implicit Approximate-Factorization Algorithm," *Journal of Computational Physics*, Vol. 39, No. 2, 1981, pp. 347–363.

[22]Steger, J. L., Ying, S. X., and Schiff, L. B., "A Partially Flux-Split Algorithm for Numerical Simulation of Unsteady Viscous Flows," *Proceedings of a Workshop on Computational Fluid Dynamics*, Univ. of California, Davis, CA, Aug. 1986.

[23]Ward, K., and Katz, J., "The Interaction Between Primary and Secondary Flow Structures in the Lee of an Inclined Body of Revolution," AIAA Paper 89-0143, Jan. 1989.

[24]Pagan, D., and Molton, P., "Basic Experiment on a Supersonic Vortex Flow Around a Missile Body," AIAA Paper 91-0287, Jan. 1991.

[25]Ying, S. X., Schiff, L. B., and Steger, J. L., "A Numerical Study of Three-Dimensional Separated Flow Past a Hemisphere Cylinder," AIAA Paper 87-1207, June 1987.